Near-to-Far Field Transformation in FDTD: A Comparative Study of Different Interpolation Approaches

Ravi C. Bollimuntha[1], Mohammed F. Hadi[2], Melinda J. Piket-May[1], Atef Z. Elsherbeni[2]

[1]Department of Electrical, Computer and Energy Engineering
University of Colorado Boulder, Boulder, CO 80309, USA
ravi.bollimuntha@colorado.edu, mjp@colorado.edu

[2]Department of Electrical Engineering
Colorado School of Mines, Golden, CO 80401, USA
mhadi@mines.edu, aelsherb@mines.edu

Abstract—Equivalence theorems in electromagnetic field theory stipulate that farfield radiation pattern/scattering profile of a source/scatterer can be evaluated from fictitious electric and magnetic surface currents on an equivalent imaginary surface enclosing the source/scatterer. These surface currents are in turn calculated from tangential (to the equivalent surface) magnetic and electric fields, respectively. However, due to the staggered-in-space placement of electric and magnetic fields in FDTD Yee cell, selection of a single equivalent surface harboring both tangential electric and magnetic fields is not feasible. The work-around is to select a closed surface with tangential electric (or magnetic) fields and interpolate the neighboring magnetic (or electric) fields to bring approximate magnetic (or electric) fields onto the same surface. Interpolation schemes available in the literature include averaging, geometric mean and the mixed-surface approach. In this work, we compare FDTD farfield scattering profiles of a dielectric cube calculated from surface currents that are obtained using various interpolation techniques. The results are benchmarked with those obtained from integral equation solvers available in the commercial packages FEKO and HFSS.

Index Terms— Bistatic RCS, Equivalence theorem, FDTD, Field interpolation, Near-to-farfield transformation, Total-field/Scattered-field (TF/SF).

I. INTRODUCTION

Equivalence theorems come very handy in efficiently calculating farfields from a radiating source or a scatterer. Extending the problem space to include the farfield region is not often computationally feasible due to time and memory costs involved. Instead, the nearfields in the form of fictitious surface currents on equivalent surface are used to calculate the farfield magnetic and electric vector potentials A and F [1]. These vector potentials are then used to obtain either radiation pattern in case of sources or radar cross section (RCS) in case of scatterers. The equivalent surface fully encloses the sources/scatterers, and small enough to keep the computational costs in budget. The whole process, called near-to-farfield transformation (NTFF), requires calculation of unknown nearfields on an equivalent surface using analytical or numerical methods depending on the problem at hand. Nearfields of complex scattering structures, such as an airplane or a vessel, can only be solved numerically using techniques such as FDTD, method of moments (MoM) and finite element method (FEM).

In FDTD, one peculiar aspect about choosing the equivalent surface is that it is not possible for any single closed surface to house both the tangential electric (E) and magnetic (H) nearfields that are used to calculate surface currents J_s and M_s. The reason being, the E and H fields are not co-located in the FDTD grid (staggered in space along all three dimensions). This makes it necessary to interpolate fields from neighboring Yee cells in order to bring E and H (and thereby J_s and M_s) onto the same surface.

Arithmetic averaging has been widely used in the literature [2–4] to interpolate and bring fields onto the same surface in the FDTD grid. Use of geometric mean [5] for interpolation is also demonstrated to yield better results for 2D scattering problems. Another radical method called the mixed-surface approach [6], that does not involve any interpolation, is also shown to perform better for strong backward-scattering problems. In

Submitted On: June 28, 2019
Accepted On: April 17, 2021

https://doi.org/10.47037/2020.ACES.J.360502

this work, we compare the bistatic RCS of a dielectric cube, obtained in FDTD using aforementioned interpolation techniques, with those obtained from integral equations solvers in commercial packages FEKO and HFSS-IE. A cube scatterer, that snaps to the electric field FDTD grid, is chosen to avoid artifacts of stair-casing in the FDTD-calculated RCS. In FEKO and HFSS-IE, the planewave source is used to illuminate the scatterer in a particular direction. In FDTD, we use the perfect total-field/scattered-field (TF/SF) technique [7–10] for planewave illumination of scatterer. The TF/SF technique used is perfect in the sense that the spurious field leakage into the scattered field region is essentially nonexistent. Moreover, it is possible to launch planewave in almost any arbitrary direction.

Frequency domain NTFF transformation is used to obtain farfield scattering profile (to be exact, bistatic radar cross section, RCS), in the three planes XY, XZ and YZ, of the dielectric cube at a single frequency. This involves applying DFT (Discrete Fourier Transform) to the time-domain surface currents (on the entire equivalent surface) to obtain frequency domain currents at the desired frequency. These frequency domain currents are then used to calculate RCS at the desired frequency.

II. LEAKAGE-FREE TF/SF TECHNIQUE FOR A PLANEWAVE SOURCE IN FDTD

In TF/SF formulation, the FDTD problem space is divided into two regions: a total-field (TF) region and a scattered-field (SF) region. The interface between the two regions is used to introduce planewave sourcing conditions that excite fields inside the TF region. This is also an application of equivalence principle, that equivalent sources are used here to recreate fields *inside* a volume bounded by a closed surface.

Exciting planewaves using TF/SF formulation involves two steps [7–10]: 1) propagate a planewave, exploiting its one dimensional nature, along an auxiliary 1D FDTD grid. 2) Use the fields computed on the auxiliary 1D grid to enforce source conditions, in the form of consistency corrections to the main grid update equations, at the interface between the TF and SF regions. These consistency corrections act as equivalent source conditions and excite the planewave in the TF region of the main grid.

If the fields on the 1D grid undergo the same numerical dispersion as that of the main grid, it is possible to perfectly confine the planewave to the TF region, without any leakage into SF region. The above condition is satisfied, as shown by [9], when $\frac{p_x \Delta x}{m_x} = \frac{p_y \Delta y}{m_y} = \frac{p_z \Delta z}{m_z} = \Delta r$ (the rational angle condition), where $p_x = \cos\phi_{inc} \sin\theta_{inc}$, $p_y = \sin\phi_{inc} \sin\theta_{inc}$, and $p_z = \cos\theta_{inc}$. The angles θ_{inc} and ϕ_{inc} specify the direction of propagation of incident planewave. m_x, m_y, and m_z are some integers (all even or all odd), and Δr is 1D grid spacing.

If we intend to excite a planewave that propagates along certain direction θ_{inc} and ϕ_{inc}, then we choose some integers that roughly satisfy the following:

$$\phi_{inc} = \tan^{-1}\frac{m_y}{m_x},\ \theta_{inc} = \cos^{-1}\frac{m_z}{\sqrt{m_x^2 + m_y^2 + m_z^2}}, \quad (1)$$

which are directly derived from the rational angle condition. Larger integers can be chosen to finely resolve the angle of incidence.

The unique feature of this process is every field location of the main grid can be mapped onto a 1D grid (along the unit propagation vector of the planewave) and vice-versa. This allows us to collapse the very 3D FDTD update equations into a 1D form, thereby ensuring the fields on the 1D grid undergo the same numerical dispersion as that of the main 3D grid. This in turn ensures that the spurious leakage into SF region is negligible (as low as $-320\ dB$ or at machine precision), as mentioned earlier.

The polarization of the planewave is defined by E_ϕ and E_θ, for example if $E_\theta = 1$ & $E_\phi = 0$, the planewave will be theta-polarized. The polarization coefficients of the electric and magnetic fields in the X, Y and Z directions are given by [4]:

$$\begin{aligned}
E_{inc,x} &= [E_\theta \cos(\tilde{\theta}_{inc}) \cos(\tilde{\phi}_{inc}) - E_\phi \sin(\tilde{\phi}_{inc})] f(t),\\
E_{inc,y} &= [E_\theta \cos(\tilde{\theta}_{inc}) \sin(\tilde{\phi}_{inc}) + E_\phi \cos(\tilde{\phi}_{inc})] f(t),\\
E_{inc,z} &= -E_\theta \sin(\tilde{\theta}_{inc}) f(t),\\
H_{inc,x} &= \frac{-1}{\eta_0}[E_\phi \cos(\tilde{\theta}_{inc}) \cos(\tilde{\phi}_{inc}) + E_\theta \sin(\tilde{\phi}_{inc})] f(t),\\
H_{inc,y} &= \frac{-1}{\eta_0}[E_\phi \cos(\tilde{\theta}_{inc}) \sin(\tilde{\phi}_{inc}) - E_\theta \cos(\tilde{\phi}_{inc})] f(t),\\
H_{inc,z} &= \frac{1}{\eta_0} E_\phi \sin(\tilde{\theta}_{inc}) f(t),
\end{aligned} \quad (2)$$

where the function $f(t)$ is a time-series having a suitable profile for FDTD simulations that rises smoothly from zero or negligible value, such as sufficiently delayed Gaussian or modulated Gaussian pulses. The above coefficients are useful when hard-sourcing few initial grid points, to initiate the planewave on the auxiliary 1D grid of the TF/SF formulation [10]. Numerical angles (with a $\tilde{}$, i.e. $\tilde{\theta}_{inc}$ and $\tilde{\phi}_{inc}$) are used to calculate these coefficients. For the relationship between numerical angles and those given in equation (1), refer to [8].

III. NTFF EQUIVALENT SURFACE FIELD INTERPOLATION TECHNIQUES

The equivalent surface, on which near-to-farfield transformation is performed, is placed in the scattered field region as shown in Fig. 1. The scattered fields on

this equivalent surface are used to calculate surface currents, that are used in the surface integrals to calculate vector potentials. However, a single equivalent surface will not house both the tangential magnetic and electric fields (or surface currents), because of the staggered field locations in FDTD grid, as shown in Fig. 2.

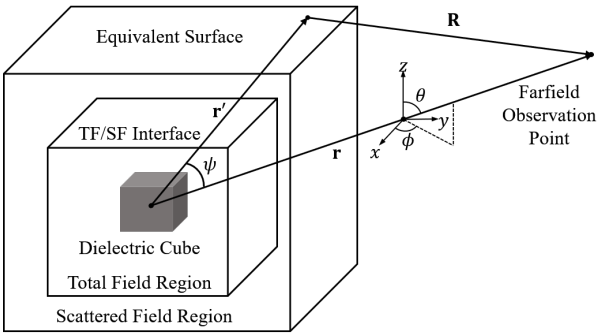

Fig. 1. Schematic of the FDTD problem space, showing the dielectric scatterer, TF/SF regions and the Equivalent surface.

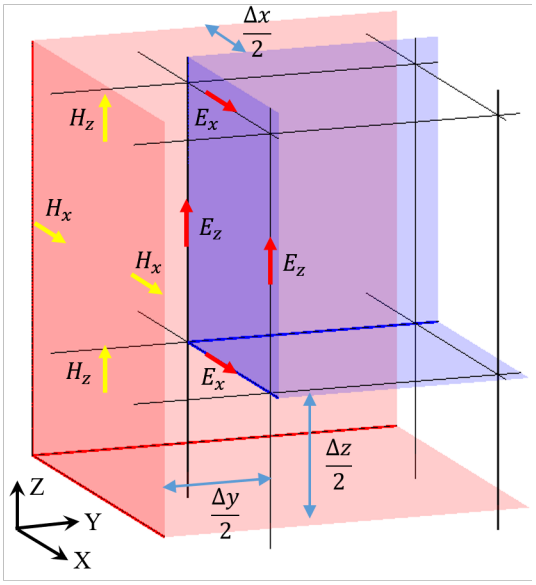

Fig. 2. The tangential electric and magnetic fields on two separate surfaces, red and blue.

One of the techniques to bring the surface currents (J_s and M_s) on to the same surface is to interpolate electric and magnetic fields using arithmetic average. Average of four H fields and two E fields (time-domain fields) brings currents onto the same surface and to the same location, as demonstrated in [4]. This is shown in Fig. 3. Discrete Fourier transform (DFT) is applied on the time-domain average to obtain frequency-domain current components, at the desired frequencies. These frequency-domain currents are obtained at discrete locations, covering all the six faces of the equivalent surface.

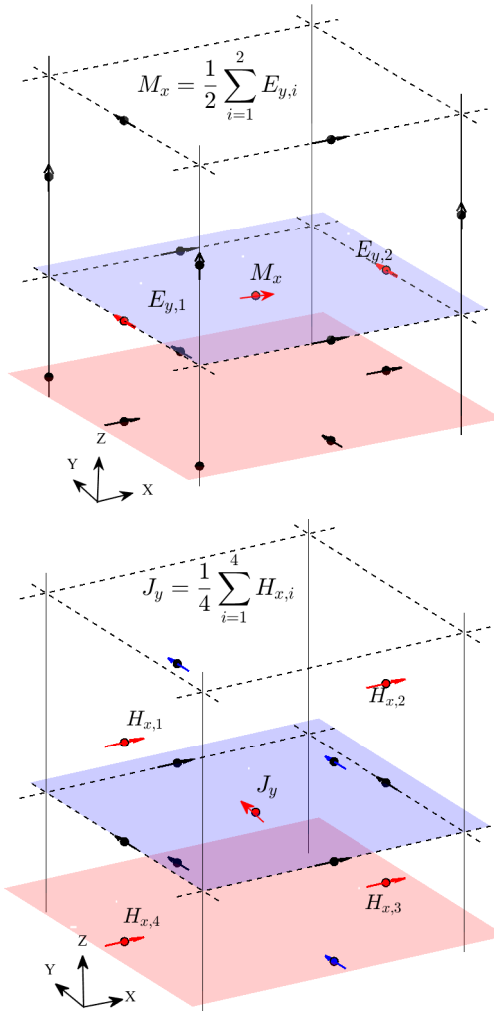

Fig. 3. Top: Average of two electric field components highlighted red gives magnetic current component M_x. Bottom: Average of four magnetic field components highlighted red gives electric current component J_y.

Geometric mean interpolation is another technique that can also be performed on the same fields as used by arithmetic averaging, shown in Fig. 3. However, a different sequence of steps is followed. First, the DFT is applied on the four time-domain H fields and the two time-domain E fields at the desired frequencies, and then the geometric mean of the complex-valued frequency-domain currents are obtained at all the discrete locations of the equivalent surface. Directly applying geometric mean on time-domain fields would force us to take the square root and fourth root of negative real values. Applying DFT first and then taking the geometric mean

would help avoid this.

While taking the geometric mean of complex numbers, the following pitfall needs to be avoided. The phases (angles of complex numbers) range between $[-\pi, \pi]$ in computational software by default. The angles that are less than $-\pi$ (such as -1.1π and -1.5π) are automatically wrapped-up by 2π (so that -1.1π becomes 0.9π and -1.5π becomes 0.5π). This makes it difficult to interpolate angles (phases) to compute geometric mean of complex numbers, since averaging the angles that are combination of wrapped-up and those that are not produces inconsistent results. This is essentially the conundrum involved in choosing the correct root while taking n^{th} root of product of n complex numbers, i.e. the geometric mean of n complex numbers. One solution to this problem is to first detect if there are any phase wraps (negative angles wrapped to positive angles) among the angles of complex numbers that we are trying to take the geometric mean of. If there aren't any phase wraps, simply use the average of phases of the complex numbers to calculate geometric mean. If there are phase wraps, we need to subtract h multiples of 2π from sum of the phases before taking the average of phases. Here, h is the number of positive phases among the complex operands for geometric mean. This allows the complex geometric mean to correctly bisect the angle between the two/four complex operands.

Geometric mean approach theoretically produces no nearfield error while interpolating fields of a planewave. This can be shown using a simple example: consider the four H fields in the bottom portion of Fig. 3. The position vectors of these four field locations starting with bottom left location and going in anti-clockwise direction are $(x, y + \frac{1}{2}\Delta y, z), (x + \Delta x, y + \frac{1}{2}\Delta y, z), (x + \Delta x, y + \frac{1}{2}\Delta y, z + \Delta z), (x, y + \frac{1}{2}\Delta y, z + \Delta z)$. Also, consider a free space planewave propagating in arbitrary direction represented in frequency domain form: $e^{-\jmath \mathbf{k}\cdot\mathbf{r}}$, here $\mathbf{k}$ is propagation vector and $\mathbf{r}$ is position vector. If we want to interpolate the planewave at the location of J_y shown in bottom portion of Fig. 3 using the geometric mean of four H fields mentioned above, we obtain:

$$
\begin{aligned}
&exp\Big(\jmath\mathbf{k}\cdot\frac{1}{4}[(x + x + \Delta x + x + \Delta x + x)\,\mathbf{a}_x \\
&+ (y + \frac{1}{2}\Delta y + y + \frac{1}{2}\Delta y + y + \frac{1}{2}\Delta y + y + \frac{1}{2}\Delta y)\,\mathbf{a}_y \\
&+ (z + z + z + \Delta z + z + \Delta z)\,\mathbf{a}_z]\Big) \\
&= exp\left(\jmath\mathbf{k}\cdot[(x + \frac{1}{2}\Delta x)\mathbf{a}_x + (y + \frac{1}{2}\Delta y)\mathbf{a}_y + (z + \frac{1}{2}\Delta z)\mathbf{a}_z]\right),
\end{aligned}
\tag{3}
$$

that is exactly the same as can be obtained by substituting the position vector $(x + \frac{1}{2}\Delta x, y + \frac{1}{2}\Delta y, z + \frac{1}{2}\Delta z)$ of J_y in the planewave representation.

Another technique to overcome the staggered-nature of planes containing tangential currents in FDTD for performing near-to-farfield transformation is mixed-surface approach introduced in [6]. Similarities exist between mixed-surface approach and TF/SF formulation. For example, the fictitious surface currents introduced at the TF/SF interface in the TF/SF formulation, in the form of consistency corrections to the FDTD update equations, where they excite equivalent planewave fields *inside* the total field region, required no interpolation. This mixed-surface approach is a dual of the TF/SF formulation, in the sense that it also does not use field interpolation to launch equivalent farfields *outside* the equivalent surface.

During the consistency corrections to the electric field in TF/SF formulation, for example, we add or subtract incident magnetic field to the right hand side of the update equation. This is analogous to placing a magnetic field-generated electric surface current at the electric field location, i.e. shifting the location of electric surface current from the location of its associated magnetic field. Similarly, the location of magnetic surface current is changed from the location of its associated electric field. This mixing of field and current locations, when applied to near-to-farfield transformation, is referred the Mixed-Surface approach [6].

The implementations of the mixed-surface approach is shown in equations (4) and Fig. 4:

$$
\begin{aligned}
\mathbf{N} &= \oiint_{S_h} \hat{\mathbf{n}} \times \mathbf{H}|_{S_h} e^{\jmath k\hat{\mathbf{r}}\cdot\mathbf{r}'_e} dS' = \oiint_{S_h} \mathbf{J}_s|_{S_e} e^{\jmath k\hat{\mathbf{r}}\cdot\mathbf{r}'_e} dS', \\
\mathbf{L} &= -\oiint_{S_e} \hat{\mathbf{n}} \times \mathbf{E}|_{S_e} e^{\jmath k\hat{\mathbf{r}}\cdot\mathbf{r}'_h} dS' = \oiint_{S_e} \mathbf{M}_s|_{S_h} e^{\jmath k\hat{\mathbf{r}}\cdot\mathbf{r}'_h} dS',
\end{aligned}
\tag{4}
$$

where S_e and S_h represent two surfaces on which the tangential electric and magnetic fields are present, respectively, in FDTD grid. When evaluating the surface integral for $\mathbf{N}$ using the magnetic fields on S_h, the surface electric currents caused by the magnetic fields ($\mathbf{J}_s = \hat{\mathbf{n}} \times \mathbf{H}$) are assumed to be placed on S_e. Therefore, the distance (between the reference point, i.e. the center of the volume enclosed by equivalent surface, and the current location on S_e) r'_e is used in the exponential inside integral.

Similarly, when evaluating the surface integral for $\mathbf{L}$ using the electric fields on S_e, the surface magnetic currents caused by the electric fields ($\mathbf{M}_s = -\hat{\mathbf{n}} \times \mathbf{E}$) are assumed to be placed on S_h. Thus, the distance r'_h is used in the exponential term inside integral. Finally, a separate-surface approach, that does not involve any mixing of field and current location and similar to mixed-surface approach in all other aspects, is implemented.

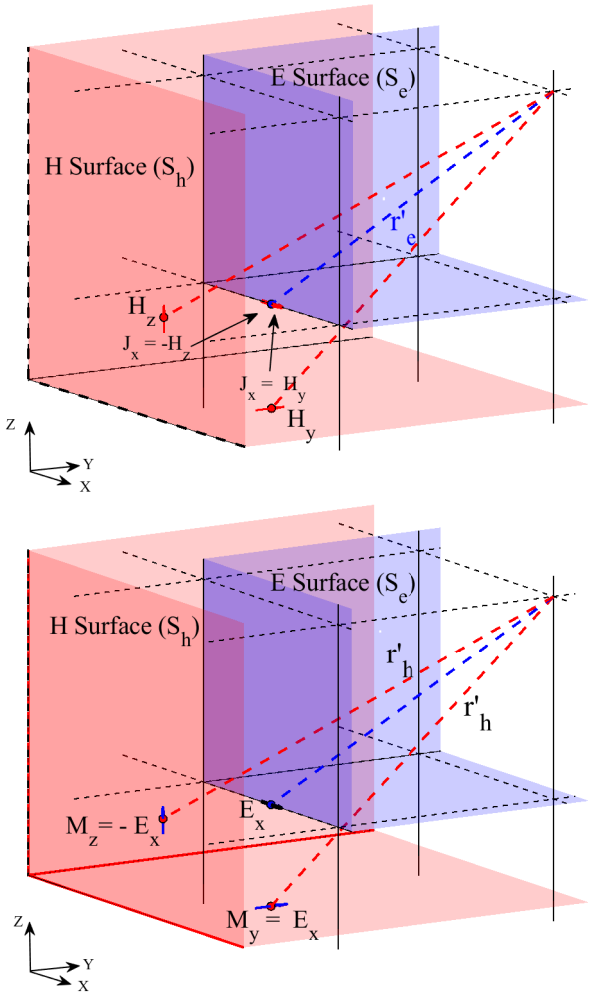

Fig. 4. Top: Magnetic field-produced electric currents are placed on S_e. Bottom: Electric field-produced magnetic currents are placed on S_h.

IV. FREQUENCY DOMAIN NEAR-TO-FARFIELD TRANSFORMATION IN FDTD

The frequency domain near-to-farfield projection is defined in terms of vector potential functions **A** and **F** in equations (5):

$$\mathbf{A}(\hat{\mathbf{r}},\omega) = \frac{\mu_0 e^{-jkR}}{4\pi R}\oiint_S \mathbf{J}_s(\mathbf{r}',\omega)e^{jk\hat{\mathbf{r}}\cdot\mathbf{r}'}dS' = \frac{\mu_0 e^{-jkR}}{4\pi R}\mathbf{N},$$
$$\mathbf{F}(\hat{\mathbf{r}},\omega) = \frac{\epsilon_0 e^{-jkR}}{4\pi R}\oiint_S \mathbf{M}_s(\mathbf{r}',\omega)e^{jk\hat{\mathbf{r}}\cdot\mathbf{r}'}dS' = \frac{\epsilon_0 e^{-jkR}}{4\pi R}\mathbf{L}. \tag{5}$$

The above equations are functions of frequency and farfield position unit vector $\hat{\mathbf{r}}$ along **r** shown in Fig. 1. The unit vector also represents farfield angles θ and ϕ. The closed surface integral is over the equivalent surface, and the frequency domain currents $\mathbf{J}_s$ and $\mathbf{M}_s$ (complex-valued) are functions of position on the equivalent surface (represented by primed position vector $\mathbf{r}'$ shown in Fig. 1) and the frequency. R is the magnitude of the vector $\mathbf{R} = \mathbf{r} - \mathbf{r}'$, also shown in Fig. 1.

The auxiliary vectors **N** and **L** in equations (5), that represent only the surface integrals, are then used to calculate the θ and ϕ components of electric field, given by equations (6):

$$E_\theta(\theta,\phi,\omega) = -\frac{je^{-jkR}}{4\pi R}\Big(L_\phi + \eta_0 N_\theta\Big),$$
$$E_\phi(\theta,\phi,\omega) = \frac{je^{-jkR}}{4\pi R}\Big(L_\theta - \eta_0 N_\phi\Big). \tag{6}$$

Similarly, the θ and ϕ components of RCS are given by equations (7):

$$RCS_\theta(\theta,\phi,\omega) = \frac{k^2}{8\pi\eta_0 P_{inc}}\Big|L_\phi + \eta_0 N_\theta\Big|^2,$$
$$RCS_\phi(\theta,\phi,\omega) = \frac{k^2}{8\pi\eta_0 P_{inc}}\Big|L_\theta - \eta_0 N_\phi\Big|^2, \tag{7}$$

where k and η_0 are the free-space wave-number and the intrinsic impedance, respectively. The surface integration in equations (5) are carried as discrete summations (Riemann sum). And, P_{inc} is the power density of the incident planewave, given by $P_{inc} = \frac{1}{2\eta}\left(E_\theta^2 + E_\phi^2\right)\cdot|F(\omega)|^2$. Here $F(\omega)$ is the Fourier transform of time-series $f(t)$, defined in equations (2), sampled at the desired frequency ω. The θ and ϕ components of the auxiliary vectors **N** and **L** are defined by equations (8) [4]:

$$N_\theta = \oiint_S \Big(J_x\cos(\theta)\sin(\phi) + J_y\cos(\theta)\sin(\phi) - J_z\sin(\theta)\Big)e^{jkr'\cos(\psi)}dS',$$
$$N_\phi = \oiint_S \Big(-J_x\sin(\phi) + J_y\cos(\phi)\Big)e^{jkr'\cos(\psi)}dS',$$
$$L_\theta = \oiint_S \Big(M_x\cos(\theta)\sin(\phi) + M_y\cos(\theta)\sin(\phi) - M_z\sin(\theta)\Big)e^{jkr'\cos(\psi)}dS',$$
$$L_\phi = \oiint_S \Big(-M_x\sin(\phi) + M_y\cos(\phi)\Big)e^{jkr'\cos(\psi)}dS'. \tag{8}$$

V. ERROR COMPARISON WITHOUT A SCATTERER

As a way to benchmark the accuracy of the above interpolation schemes, an empty region (no-scatterer) is illuminated by a planewave using discrete planewave technique with TF/SF formulation described earlier. Then, the farfields are obtained from the nearfields which are

interpolated using different schemes dealt with in the previous section, and compared. Since the fields in the scattered-field region for this case are down to the machine precision, the equivalent surface to perform NTFF transformation is placed inside the total-field region. As one might expect, the no-scatterer case should ideally result in zero farfield. Any electric farfield based on equation (6) observed is an error (the noise floor). Errors can be because of: numerical dispersion inherent in FDTD, approximations in calculation of J_s and M_s, discrete surface integration, discretization in space and time, and truncation of fields (finite word length).

Although this work does not attempt to separate the above mentioned error types, the farfield error caused by the error in approximating (interpolating) the nearfield surface currents J_s and M_s is the main differentiator. This is because, all the other error contributors mentioned above are identical for all the interpolation techniques. Therefore, it is expected that the interpolation scheme that gives minimum farfield performs better than the rest in terms of accuracy. The above interpolation schemes are compared for three different simulation parameters: resolution of the FDTD grid, incident angle of the planewave, and size of the equivalent surface.

A. Resolution sweep

Figure 5 shows how different interpolation schemes compare for different resolution of the grid. The vertical axis is the maximum of $\sqrt{|E_\theta|^2+|E_\phi|^2} \cdot \Delta t$ in dB observed across angles in the farfield principal planes (XY, XZ, and YZ planes). Here Δt is the FDTD discretization time step. The horizontal axis is the grid resolution in terms of cells per wavelength. The frequency at which the farfields are calculated is 2 GHz.

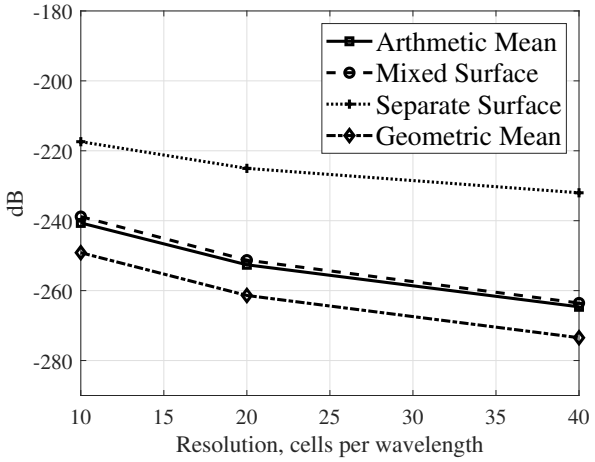

Fig. 5. Maximum farfield error in dB for different grid resolutions.

On the other hand, Fig. 6 shows average of $\sqrt{|E_\theta|^2+|E_\phi|^2} \cdot \Delta t$ observed across angles in the farfield principal planes.

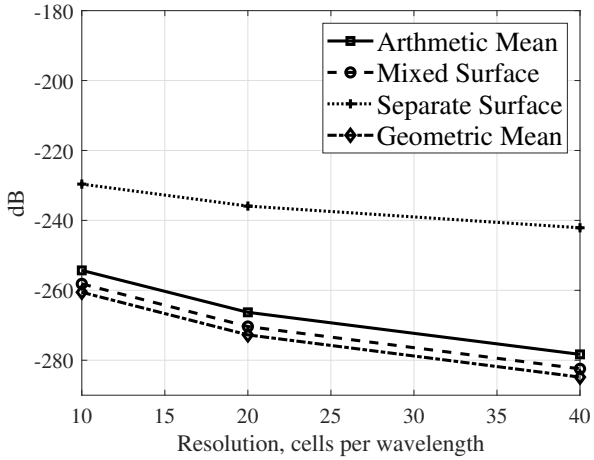

Fig. 6. Average farfield error in dB for different grid resolutions.

The incident angle for the planewave is $\phi_{inc} = 35.5^0, \theta_{inc} = 38^0$ and the size of equivalent surface is $(1\lambda)^3$. As expected, the farfield error decreases with increase in resolution as the dicretization errors in FDTD get minimized when the grid gets finer. The geometric mean approach produces the lowest farfield as one might expect because it interpolates the nearfields exactly as shown in section III, closely followed by arithmetic and mixed-surface approaches, followed by distant separate surface approach.

B. Incident angle sweep

Figures 7 and 8 show how maximum and average errors compare for different interpolation schemes at different incident angles of the planewave. The vertical axis is the same as described before and the horizontal axis specifies the θ_{inc} direction of the planewave while the $\phi_{inc} = 23.2^0$. The size of the equivalent surface is $(5\lambda)^3$ and the grid resolution is 10 cells per wavelength. The frequency at which the farfields are calculated is 2 GHz. The trend suggests that as incident planewave direction gets close to the axes directions ($\theta_{inc} = 0, 90^0$), the farfield errors increase. This could be because of FDTD numerical dispersion errors becoming worse for waves propagating along the axes directions as demonstrated in [11].

C. Equivalent surface size sweep

Figures 9 and 10 show how maximum and average errors compare for different interpolation schemes for different equivalent surface sizes. The vertical axis is same as described before and the horizontal axis specifies the size of equivalent surface as multiple of λ in $6(n\lambda)^2$.

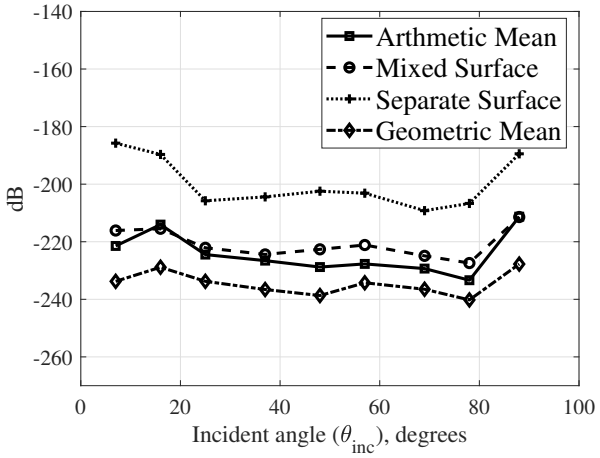

Fig. 7. Maximum farfield error in dB for different planewave incident angles.

The incident angle for the planewave is $\phi_{inc} = 35.5^0$, $\theta_{inc} = 38^0$, and the grid resolution is 10 cells per wavelength. The frequency at which the farfields are calculated is 2 GHz. Again, the geometric mean performs best, while arithmetic and mixed-surface approaches perform better than separate surface approach.

As expected, the farfield errors increase as size of equivalent surface increases. This is because, the phase errors in FDTD accumulate more as the wave travels in the grid longer and longer. All the above comparisons show that the geometric mean, mixed surface and arithmetic mean interpolation schemes perform consistently and considerably better when compared to the separate surface approach. Importantly, the geometric mean approach produces minimum farfield error, and the arithmetic & mixed surface approach produce similar errors.

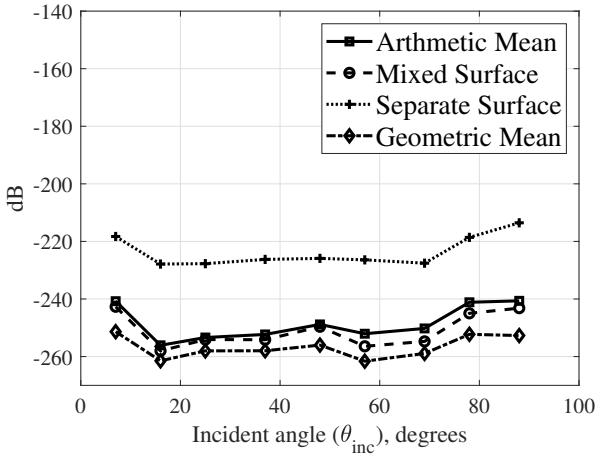

Fig. 8. Average farfield error in dB for different planewave incident angles.

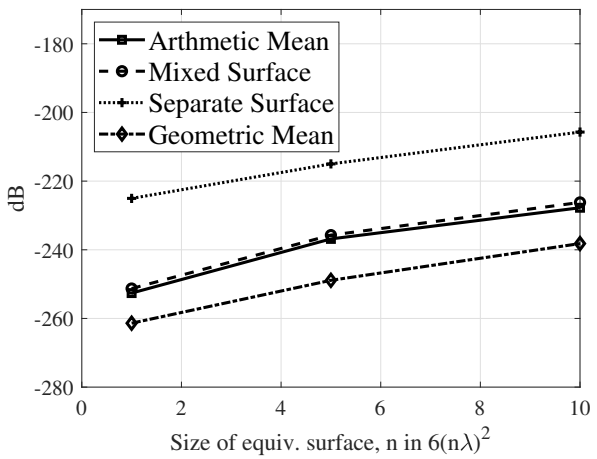

Fig. 9. Maximum farfield error in dB for various equivalent surface sizes.

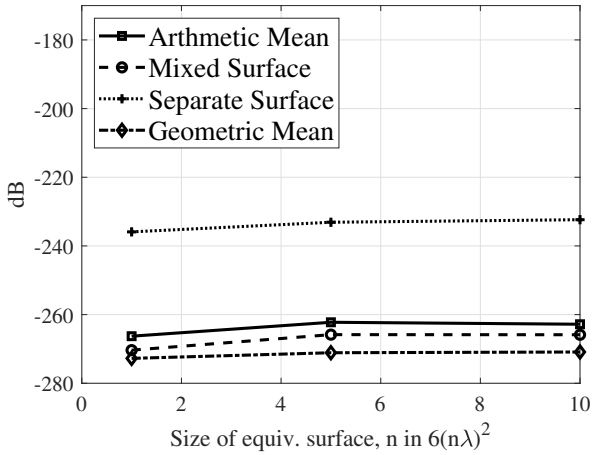

Fig. 10. Average farfield error in dB for various sizes of equivalent surface.

VI. BISTATIC RCS COMPARISON FOR A DIELECTRIC CUBE

To further validate the performance of different FDTD interpolation schemes, the bistatic RCS of a dielectric cube ($\epsilon_r = 5, \mu_r = 1$) is calculated at a single frequency of 1 GHz. This FDTD farfield scattering profile is compared with those obtained from integral equation solvers available in FEKO and HFSS.

The auxiliary vectors **N** and **L** in equations (5), that represent only the surface integrals, are used to calculate the θ and ϕ components of RCS, given by equations (7). The dielectric cube of size $\lambda/2$ on each side (at 1 GHz) is illuminated with a planewave incident at $\theta_{inc} = 38.0^0$ and $\phi_{inc} = 35.5^0$. This incident angle is rendered by the choice of integers (m_x,m_y,m_z) as (7,5,11) in the perfect TF/SF formulation described in the initial sections. These angles in FDTD indicate the direction of planewave propagation (direction of propagation

vector). Contrary to this, HFSS and FEKO would require the direction the planewave comes from (opposite to the direction of propagation vector). Consequently, the planewave arrival angles, $\theta_{arrival} = 180 - \theta_{inc}$ and $\phi_{arrival} = 180 + \phi_{inc}$, are used in these solvers. The time-profile of the theta-polarized planewave is a modulated Gaussian pulse, with frequency spectrum centered around 1 GHz.

The RCS results from the four interpolation schemes of interest –arithmetic averaging, geometric mean, mixed-surface, separate-surface approach– are compared with RCS profiles obtained from FEKO-MoM and HFSS-IE in Fig. 11.

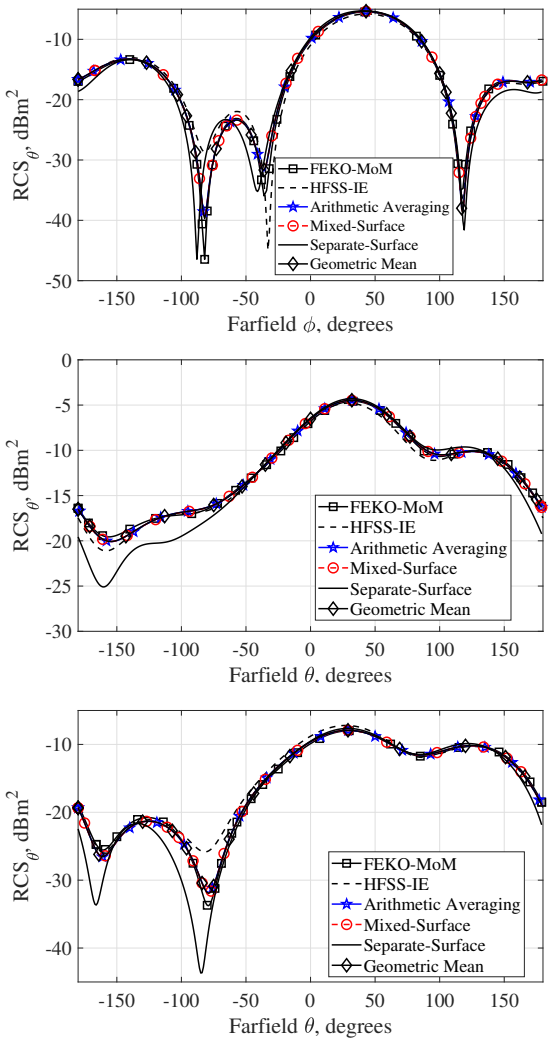

Fig. 11. The θ component of bistatic RCS in different farfield planes (XY, XZ and YZ respectively).

These figures show that the geometric mean, mixed surface and arithmetic averaging schemes match very close to each other and to at least one integral equation solution (FEKO in this case) confirming the clear advantage they have over the separate surface approach. Here, the FDTD grid resolution used is 40 cells/wavelength at 1 GHz. Also, only RCS_θ is shown on the three farfield principal planes as the RCS_ϕ results do not deviate from each other to a perceivable degree. The absorbing boundary condition used is Convolutional Perfectly Matched Layer (CPML) for the simulations involving dielectric cube. The CPML depth is 10 cells and there is a 10-cell gap between NTFF equivalent surface and CPML. The dielectric cube case is presented as a practical case to show how the errors in the FDTD NTFF formulation manifest themselves in RCS for different interpolation schemes, while keeping all other conditions (including type of ABC and distance to ABC) exactly same. No significant difference is observed between FDTD results (obtained using geometric mean, arithmetic averaging, mixed-surface approaches) and MoM-based FEKO results as shown in this section.

VII. SUMMARY AND CONCLUSION

Four interpolation approaches (arithmetic averaging, mixed-surface, geometric mean and separate surface scheme) for performing the frequency-domain near-to-farfield transformation in 3D FDTD are compared in terms of their baseline farfield errors and bistatic RCS for a dielectric cube. The planewave is excited in the FDTD grid using the error-free total-field/scatterd-field technique. To establish the baseline for farfield error comparison, nearfields without any scatterer in the total-field region are transformed to farfields. In this comparison, the geometric mean interpolation produces minimum farfield error as expected, followed by competing arithmetic averaging and mixed surface approaches, while the separate surface approach produces maximum error. Also, the FDTD RCS profiles calculated using geometric mean, arithmetic averaging and mixed-surface approaches for a dielectric cube match very close with that calculated using integral equation technique.

REFERENCES

[1] C. A. Balanis, *Advanced Engineering Electromagnetics*. New York: John Wiley, 1989.

[2] R. J. Luebbers, K. S. Kunz, M. Schneider, and F. Hunsberger, "A Finite-Difference Time-Domain Near Zone to Far Zone Transformation," *IEEE Trans. Antennas Propag.*, vol. 39, no. 4, pp. 429–433, Apr. 1991.

[3] M. J. Barth, R. R. McLeod, and R. W. Ziolkowski, "A Near and Far-Field Projection Algorithm for Finite-Difference Time-Domain Codes," *J. Electromagn. Waves Appl.*, vol. 6, no. 1, pp. 5–18, 1992.

[4] A. Z. Elsherbeni and V. Demir, *The Finite Difference Time Domain Method for Electromagnetics*

with MATLAB Simulations, 2nd ed., ACES Series on Computational Electromagnetics and Engineering, SciTech Publishing Inc. an Imprint of the IET. Edison, NJ, 2015.

[5] D. J. Robinson and J. B. Schneider, "On the use of the geometric mean in FDTD near-to-far-field transformations," *IEEE Trans. Antennas Propag.*, vol. 55, no. 11, pp. 3204–3211, Nov. 2007.

[6] T. Martin, "An improved near- to far-zone transformation for the finite-difference time-domain method," *IEEE Trans. Antennas Propag.*, vol. 46, no. 9, pp. 1263–1271, Sep. 1998.

[7] T. Tan and M. Potter, "1-D multipoint auxiliary source propagator for the total-field/scattered- field FDTD formulation," *IEEE Antennas Wirel. Propag. Lett.*, vol. 6, pp. 144–148, 2007.

[8] M. F. Hadi, "A Versatile Split-Field 1-D Propagator for Perfect FDTD Plane Wave Injection," *IEEE Trans. Antennas Propag.*, vol. 57, no. 9, pp. 2691–2697, Sep. 2009.

[9] T. Tan and M. Potter, "FDTD Discrete Planewave (FDTD-DPW) Formulation for a Perfectly Matched Source in TFSF Simulations," *IEEE Trans. Antennas Propag.*, vol. 58, no. 8, pp. 2641–2648, Aug. 2010.

[10] R. C. Bollimuntha, M. F. Hadi, M. J. Piket-May, and A. Z. Elsherbeni, "Dispersion optimised plane wave sources for scattering analysis with integral based high order finite difference time domain methods," *IET Microwaves, Antennas Propag.*, vol. 10, no. 9, pp. 976–982, 2016.

[11] A. Taflove and S. Hagness, *Computational Electrodynamics: The Finite-Difference Time-Domain Method, 3 ed.* Boston, MA: Artech House, 2005.